Quiescence-inducing 3D-engineered matrix uncovers mechanosensitive and drug protective FHL2-p21 signaling axis

Sadra Bakhshandeh[1], Hubert M. Taïeb[1], Adithi R. Varadarajan[2], Susanna M. Lissek[3], Sarah M. Hücker[2], Xin Lu[2], Daniela S. Garske[1], Sarah A. E. Young[1], Jörg Contzen[4, 5, 6], Manfred Gossen[5, 6], Stefan Kirsch[2], Jens Warfsmann[2], Kamran Honarnejad[2], Christoph A. Klein[2, 3], Amaia Cipitria[1, 7, 8*]

[1]Department of Biomaterials, Max Planck Institute of Colloids and Interfaces, Potsdam, Germany

[2]Division of Personalized Tumor Therapy, Fraunhofer Institute for Toxicology and Experimental Medicine, Regensburg, Germany

[3]Experimental Medicine and Therapy Research, University of Regensburg, Regensburg, Germany

[4]Department of Experimental Neurology, Charité - Universitätsmedizin Berlin, Berlin, Germany

[5]Institute of Active Polymers, Helmholtz-Zentrum Hereon, Teltow, Germany

[6]Berlin-Brandenburg Center for Regenerative Therapies, Charité Campus Virchow Klinikum, Berlin, Germany

[7] Group of Bioengineering in Regeneration and Cancer, Biodonostia Health Research Institute, San Sebastian, Spain

[8]IKERBASQUE, Basque Foundation for Science, Bilbao, Spain

Correspondence to: amaia.cipitria@mpikg.mpg.de

Abstract

Resected tumors frequently relapse with distant metastasis, despite systemic treatment. Cellular quiescence has been identified as an important mechanism underlying such drug resistance enabling late relapse. Nonetheless, hurdles associated with detection and isolation of disseminated cancer cells (DCCs) in disease-free patients urge the need for *in vitro* models of quiescent cells suited for drug screening campaigns. Here, we explore a quiescence-inducing 3D-engineered matrix based on ultraviolet light-initiated thiol-ene-crosslinked alginate hydrogels, which generate mechanical confinement and induce growth arrest and survival against chemotherapy in cancer cells. As underlying mechanism, we identified stiffness-dependent nuclear localization of the four-and-a-half LIM domains 2 (FHL2) protein, leading to p53-independent high $p21^{Cip1/Waf1}$ nuclear expression, validated in murine and human tissue. Suggestive of a resistance-causing role, cells in the quiescence-inducing matrix became sensitive against chemotherapy upon FHL2 downregulation. Thus, our biomaterial-based approach will enable systematic screens for novel compounds suited to eradicate potentially relapsing, dormant cancer cells.

Introduction

Most cancer-associated deaths are due to metastasis, with eventual relapses spanning from years to decades despite adjuvant and chemotherapies(*1*, *2*). Cancer dormancy has been described as one of the main mechanisms of evasion, which, due to its asymptomatic nature, poses significant technical and ethical challenges for the identification, isolation and investigation of DCCs(*3*). This calls for reliable *in vitro* culture systems to mimic this geno/phenotypic state to finally enable scalable drug screening campaigns for the identification of promising target drugs. Material-based, bioengineered-niche approaches have been previously pursued to induce and/or preserve the quiescence of astrocytes(*4*) and muscle stem cells(*5*), maintain neural progenitor(*6*) and hematopoietic cell stemness(*7*), investigate mechanical memory(*8*) and differentiation of stem cells(*9*), as well as to investigate cancer cell cycle progression(*10*, *11*). Here, we harnessed a similar approach by developing ultraviolet (UV) light-initiated, thiol-ene-mediated, covalently-crosslinked alginate hydrogels, which through 3D mechanical confinement induce and maintain large populations of single breast cancer cells in a growth-arrested state. We showed that artificial quiescence-inducing matrices select for distinct populations of growth-arrested cells, with cells in the G_0/G_1 cell cycle phase being more resistant to confinement. Combined with RNA sequencing, we revealed a stiffness-dependent nuclear localization of the four-and-a-half LIM domains 2 (FHL2) protein as an underlying mechanism of quiescence, leading to a p53-independent high $p21^{Cip1/Waf1}$ nuclear expression, validated in murine and human tissue. Suggestive of a growth arrest-mediated drug resistance, quiescent cells became sensitive against drug treatment upon FHL2 downregulation. This biomaterial-based approach with mechanically-induced quiescent cancer cells offers therapeutic applications as a simple and scalable method, to investigate large populations of dormant cancer cells, otherwise rare and inaccessible in large numbers from clinical settings, and for high throughput drug screens of novel compounds to eradicate potentially relapsing DCCs.

Results

3D mechanical confinement via covalently-crosslinked alginate yields distinct fractions and populations of growth-arrested cells based on hydrogel composition

Building on the now widely acknowledged role of the ECM in cancer induction and progression(*12*, *13*), we employed a versatile ECM-mimicking hydrogel encapsulation approach to investigate the effect of ECM-mediated 3D mechanical confinement on cell cycle progression. We used ultraviolet (UV) light-initiated thiol-ene-crosslinked alginate(*14*), an inherently inert hydrogel (non-cell adherent and non-degradable) which allows for selective modulation of parameters such as stiffness, cell adhesion or degradation (Fig.1a). Cells were encapsulated in the presence (or absence) of adhesion ligands (RGD), within degradable matrix metalloproteinases (MMP)-sensitive or non-degradable dithiothreitol (DTT)-crosslinked hydrogels (Fig.1a and Supp.Fig.1). The stiffness of the hydrogels ranged between 0.5-13kPa as a function of crosslinker concentration (Fig.1b). To monitor cell cycle progression in real-time, we genetically modified widely-used triple-negative MDA-MB-231 (MDA231) and luminal MCF7 breast cancer cell (BCC) lines, known to disseminate to secondary organs in *in vivo* models, with the fluorescence-ubiquitination-based cell cycle indicator 2 (FUCCI2)(*15*, *16*) (Fig.1c). Time-lapse imaging of MDA-FUCCI2 cells encapsulated within alginate hydrogels of different stiffness (soft for 1kPa and stiff for 10kPa), adhesion and degradation properties, as well as on two-dimensional tissue culture plastic (2D-TCP) and in 3D Matrigel, was performed over a period of 4-5 days, followed by quantification of the cell cycle state at the experimental endpoint (Fig.1d, Supp.Mov.1). 3D Matrigel and 2D TCP yielded highly proliferative (Ki67+) and metabolically active cells (resazurin reduction) in the form of 3D spheroids and single cells, respectively (Fig.1d, Supp.Fig.2b,d). Cells within the 3D alginate groups remained mostly as single cells, with the highest fraction of $S/G_2/M$ phase cells being in the soft

group, while the stiff adherent (RGD) and degradable (MMP-sensitive) groups displayed a lower percentage of $S/G_2/M$ and higher fraction of G_0/G_1 phase cells (Fig.1d). 3D alginate stiff yielded the highest fraction of cell cycle-arrested cells over 5 days (Fig.1d), while preserving high viability (Supp.Fig.2a). Interestingly, we noticed different sub-populations of cell cycle-arrested cells as a function of the expression (or lack of) of the licensing factor cdt1 (G_0/G_1 cdt1+/–; Fig.1d, Fig.2a, Supp.Mov.2-7). A recent mapping of protein dynamics during cell cycle progression revealed that the expression patterns of cdt1 is highly dynamic and distinctive of different levels of quiescence, with the lowest (cdt1-) identifying a longer time spent in a growth-arrested state(*17*). MDA231 cells in quiescence-inducing alginate stiff hydrogels displayed higher resistance to chemotherapy compared to cells in proliferation-permissive 3D Matrigel (Supp.Fig.2e) and, reminiscent of post-therapeutic relapses in clinical settings, were able to exit the growth-arrested state and resumed proliferation when retrieved from the hydrogels and seeded on 2D TCP (Supp.Fig.2c).

Dynamics of cell cycle and viability correlation reveal that G_0/G_1 cells are substantially more resistant to 3D mechanical confinement than cells in the $S/G_2/M$ phase

To understand the dynamics of 3D mechanical confinement-induced growth arrest, we tracked single-cell MDA-FUCCI2 fluorescence intensity (f.i.) within stiff hydrogels. Cells which were in the G_0/G_1 state at the time of encapsulation, had either lost (cdt1-) (Fig.2a1, b) or kept (cdt1+) (Fig.2a2, b) their fluorescence by the end of the experiment. On the other hand, in almost every cell initially in the $S/G_2/M$ phase, we observed a decrease in f.i. within the first few hours after encapsulation (Fig.2a3, b). By correlating cell's FUCCI2 imaging and *in situ* viability staining (calcein+; Fig.2c), we revealed that the vast majority of viable cells at day 5 were initially in the G_0/G_1 cycle state (Fig.2c, d). We validated these results for MCF7-FUCCI2 cells (Fig.2d), confirming that cells in the G_0/G_1 state are more resilient to 3D mechanical confinement compared to cells in the $S/G_2/M$ phase.

Gene expression analysis of cells in quiescence-inducing versus proliferation-permissive 3D matrices

We then looked into the gene expression of quiescence-induced cells in more details. RNA-sequencing on live cells retrieved from 3D alginate stiff (Fig.3a) revealed enrichment of cell cycle and retinoblastoma-associated molecular pathways (Fig.3b-d, Supp.Fig.3, 4), as well as regulation of senescence, autophagy and apoptosis processes when compared to cells retrieved from 3D Matrigel. In particular, we noticed strong enrichment of inflammatory response-associated pathways (TNF, NFkB and IL-17 signaling) and DNA damage stimuli response (ATM, p53 and miRNA regulation of DNA damage) (Fig.3b-e, Supp.Fig.3, 4). Intriguingly, we noticed that despite increased mRNA expression of *cdkn1a* (coding for the p21 protein) upon culture in 3D alginate stiff compared to 3D Matrigel, the levels of its key upstream cell cycle regulator *p53* is lower (Fig.3e), hinting to a potential p53-independent mechanism regulating p21 expression(*18*). This matches the lack of correlation of p53-p21 observed in patients with estrogen receptor negative (ER-) breast cancer (Supp.Fig.5). Noticing the particularly high levels of p21 (*cdkn1a*) expression among other genes in 3D alginate (Fig.3e) and its relevance in cell cycle regulation, we decided to investigate the role of p21 in regulating mechanically-induced cancer cell cycle arrest in more detail.

p21 and FHL2 localization in 3D matrices is stiffness-dependent and FHL2 mediates p21 localization and Ki67 expression

Despite the now widely acknowledge advantages of 3D vs. 2D culture systems in studying physiologically-relevant cellular processes(*19*), the role of dimensionality in the expression, localization and function of p21 remains underexplored. This is of utmost importance considering that in cancer cells the p21 oncogenic vs. suppressing function is known to depend on its level of expression and intracellular localization(*18*). We therefore assessed these features across different

3D culture systems, focusing on soft and stiff 3D alginate hydrogels. As expected, the fraction of p21-positive cells was significantly higher in 3D alginate stiff compared to soft or 3D Matrigel (Supp.Fig.6), accompanied by strong enrichment of DNA repair-associated pathways (Fig.4a-b and Supp.Fig.7). Importantly, cells in 3D alginate stiff revealed a significantly higher nuclear vs. cytoplasmic (nuc./cyto. ratio) localization of p21 compared to the soft group, together with a lower fraction of proliferative cells (Ki67 expression) (Fig.4c). Inhibiting MEK/ERK, PI3K/Akt and JNK, as some of the major signaling pathways regulating cell proliferation, displayed a strong effect on p21 localization (Fig.4d).

Previous work on 2D cultures had found that, in MDA231 cells, p21 is induced in response to treatment with DNA damaging drugs such as doxorubicin, and this is mediated by FHL2 in a p53-independent manner(*20*). Notably, FHL2 was shown to be stably expressed in only a small subset of BCC lines with MDA231 being among the highest(*20*). Nonetheless, FHL2 localization and functional role in physiologically-relevant 3D cultures had not been addressed. We therefore investigated the nuc./cyto. ratio of FHL2 in 3D stiff compared to soft alginate hydrogels. Surprisingly, and in stark contrast to 2D cultures where soft 2D substrates lead to nuclear accumulation of FHL2(*21*), we observed a significantly higher expression and nuc./cyto. ratio of FHL2 in 3D stiff compared to soft alginate hydrogels (Fig.4e). This effect was mitigated by inhibiting MEK/ERK and PI3K/Akt pathways but not JNK (Fig.4f). Importantly, knock-down of FHL2 revealed a decrease in p21 nuclear localization in 3D stiff hydrogels (Fig.4g), as well as an increase in proliferation activity (Ki67; Fig.4f), pointing to FHL2 being upstream of p21. The correlated expression of *cdkn1a* and *FHL2* is also found in tumor samples of patients with ER-breast cancer (Supp.Fig.8).

FHL2 knockdown sensitizes cells to chemotherapy

We then investigated whether FHL2 knockdown sensitizes cells to chemotherapy. FHL2-silenced cells in 3D alginate stiff displayed higher viability and metabolic activity than wild-type MDA231 when untreated (vehicle) (Fig.5a). Upon exposure to mitosis-blocking chemotherapeutic Paclitaxel in a concentration-dependent fashion (0.01-0.5mM), a significant reduction in viability and metabolic activity was observed (Fig.5a), pointing to a chemo-sensitizing effect upon FHL2 knockdown.

FHL2 expression and localization in murine tissue, human primary breast tumor and human early DCCs

Finally, to assess the implications for human disease, we investigated FHL2 expression and localization in a preclinical mouse model with metastatic breast cancer and in human primary tumor biopsies. Remarkably, single quiescent MDA231 cells (bone-tropic 1833 subclone) spontaneously disseminated to the mouse femur revealed nuclear FHL2, as opposed to proliferative clusters with cytoplasmic FHL2 (Fig.5b, Supp.Fig.9). Similarly, human tissue biopsies of breast tumor reveal a primarily cytoplasmic/membranous localization of FHL2 (Fig.5c), matching our observation in 3D Matrigel (Fig.5d). Furthermore, we investigated human early DCCs of an M0 breast cancer patient, with only microscopy evidence of metastasis and no clinical or radiographic evidence of distant metastasis. Disseminated breast cancer cells (cytokeratin+, an epithelial marker) in the sentinel lymph node displayed varying FHL2 signal intensity suggestive of functional heterogeneity (Fig.5e, f).

To sum up, ligand-rich, proliferation-permissive microenvironments maintain FHL2 in the membranous regions, whereas in low or non-adherent microenvironments the increase in mechanical confinement (stiffness) results in FHL2 translocation to the nucleus, leading to high p21 nuclear expression, cell cycle arrest and chemo-resistance (Fig.6).

Discussion

In this study, we use a 3D quiescence-inducing engineered matrix to investigate a mechanism of chemoresistance in mechanically-induced dormant BCCs. Systematic tuning of three variables (adhesion via RGD, degradability through MMP-sensitive crosslinkers and stiffness) enables generation of different fractions of cell populations with defined and controllable cell cycle status. Here, we harness this approach and reveal a stiffness-dependent nuclear localization of the FHL2 protein which leads to p53-independent nuclear expression of p21 as a quiescence and resistance-conferring mechanism. We further show that the expression and localization of both p21 and FHL2 in 3D to be strikingly different than previously-reported 2D studies, where FHL2 shuttling to the nucleus was shown to be substrate rigidity-dependent, such that on soft surfaces (as opposed to stiff substrates where mechanical tension is higher) it would translocate to the nucleus and induce p21 expression(*21*). In contrast, in 3D matrices ligand-rich environments such as in basement membrane matrices or primary breast tumor sites, FHL2 accumulates in adhesion sites(*21*), whereas loss of adhesion (occurring in intrinsically non-adherent materials such as alginate), results in FHL2 release from sub-membranous regions and shuttling to cytoplasmic (soft alginate) and nuclear (stiff alginate) regions. This cascade leads to p21 nuclear expression, cell cycle arrest and drug resistance for the latter (Fig.5e). Such dimensionality-dependent behavior has been similarly reported for YAP mechanotransduction in the context of breast tumor progression(*22*) and stem cell fate(*23*). Thus, it is critical to take into account the context-dependent role of the FHL2-p21 signaling axis, given its potential dual oncogenic vs. suppressive function(*18*, *24*). Notably, omission of adhesion ligands in our quiescence-inducing matrix was intentional, stemming from recent *in vivo* observations(*25*) where single DCCs were shown to reside in a dormant state with expressed but not engaged integrin receptors. Other studies have similarly observed DCCs expressing low levels of adhesion molecules(*26*), and integrin activation being a central mediator leading to their awakening(*26–29*).

FHL2 has been previously shown to concentrate at RNA polymerase (Pol) II sites(*21*), inducing c-Jun, IL6 and IL8 transcription. This is reflected in our sequencing data by the strong enrichment of RNA Pol II associated genes, with JUN, IL6 and IL8 being among the top ten (out of 9427) differentially regulated genes in the alginate stiff group (Fig.3b-e). This is in line with a recent study showing IL6 pathway activation in patient-derived early disseminated BCC in bone marrow(*30*).

To further support our findings, we investigated breast cancer cells disseminated to the bone in a metastasis mouse model, human tissue biopsies of primary breast cancer and early DCCs of an M0 breast cancer patient. Here we noted nuclear FHL2 localization in single dormant DCCs (Fig.5b) as opposed to cytoplasmic FHL2 corresponding to high proliferation activity (Ki67+) in a mouse model of breast cancer metastasis (Fig 5b). Likewise, cytoplasmic/membranous FHL2 is observed in human primary breast tumor biopsies (Fig.5c) matching the findings of proliferating cancer cells in 3D Matrigel (Fig. 5d). This is in agreement with screenings of normal and malignant human breast tissues revealing higher FHL2 expression for the latter, as shown in previous studies(*20*, *31*) and UALCAN database, while high FHL2 expression in ER- patients is associated with lower relapse-free survival rate (Supp.Fig.10). A number of disseminated breast cancer cells (cytokeratin+) were found in the sentinel lymph node both as single cells (Fig. 5e) and within cell clusters (Fig. 5f). We noted a substantial heterogeneity among the DCCs, further supporting the notion that various phenotypes exist in patients that may require different targeting approaches.

To conclude, we identify a stiffness-mediated FHL2 signaling mechanism in 3D bioengineered matrices inducing breast cancer cell quiescence and drug resistance, which recapitulates several aspects of patient-derived DCCs and mouse models of metastasis. Further, this approach can be exploited to generate large populations of single growth-arrested cells for simple,

fast and potentially scalable drug screening, since these are known to be rare and inaccessible in large numbers from clinical settings.

Materials and Methods

Synthesis of peptide-crosslinked alginate hydrogels

Norbornene-modified alginate hydrogels with thiol-ene crosslinking were synthesized as previously described(*32*). Briefly, high molecular weight (265 kDa; HMW), high guluronic acid, sodium alginate (Pronova MVG; NovaMatrix) was dissolved at 1% w/v in 0.1 M 2-(N- morpholino)ethanesulfonic acid (MES; Sigma-Aldrich), 0.3M NaCl (EMD Millipore) buffer (pH 6.5) overnight at room temperature. N-hydro-xysuccinimide (NHS; Sigma-Aldrich), followed by 1-ethyl-3-(3-dimethylami-nopropyl)-carbodiimide hydrochloride (EDC; Sigma-Aldrich) were added drop-wise at 5000 molar equivalents to the alginate solution while stirring. To functionalize the alginate backbone with norbornene functional groups, 5-norbornene-2-methylamine (TCI Deutschland GmbH) was added at a theoretical degree of substitution (DStheo) of 300 molecules per alginate chain. The final concentration of both reactions was 0.6% w/v and was run while stirring at 700 rpm at room temperature for 20 h. Next, the solution was quenched by adding hydroxylamine (Sigma-Aldrich), followed by dialysis (Spectra/Por 6, MWCO 3.5 kDa; Spectrum) against a salt gradient (6 g/L to 0 g/L; Sigma-Aldrich) in ddH_2O for 3 days with 3-4 changes per day. The solution was then purified with activated charcoal (Sigma-Aldrich), sterile-filtered (0.22 µm; Steriflip-GP; Merck) and lyophilized. To assess the actual degree of substitution, NMR measurements were performed using an Agilent 600 MHz PremiumCOMPACT equipped with Agilent OneNMR Probe (256 scans), with samples dissolved at a final concentration of 1.5% w/v in deuterium oxide (D_2O) (Supp. Fig 1b, c).

Casting of peptide-crosslinked alginate hydrogels

For hydrogel casting, the VPMS↓MRGG sequence was chosen as the enzymatically-degradable peptide crosslinker (↓ denotes the MMP cleavage site), ordered from WatsonBio Sciences at 98% purity with trifluoroacetic acid removal (Supp. Fig 1d). Double-cysteine containing dithiothreitol (DTT, Sigma-Aldrich, 43816) was used as the non-degradable crosslinker. Before casting, norbornene-modified alginate and the photoinitiator (Irgacure 2959; Sigma-Aldrich) were dissolved in phosphate-buffered saline (PBS) overnight at 50 °C under shaking. Alginate and photoinitiator concentrations were kept at 2 and 0.5% w/v respectively. The concentration of the crosslinker was changed to yield hydrogels with different mechanical properties. After mixing, the solution was pipetted with positive-displacement pipettes on a glass plated and covered with a dichloromethylsilane-coated glass slide (≥99.5%; Sigma-Aldrich). To initiate thiol-ene crosslinking, the mixture was exposed to UV light (365 nm at 10 mW/cm^2, OmniCure S2000) by placing the gel sheet in a custom-built curing chamber for 10 min. Gels were then punched out using biopsy punches of 4-6 mm (Integra Miltex) and washed with PBS until further use. To render norbornene-modified alginate adherent, a thiol-containing RGD sequence (CGG- GGRGDSP; Peptide 2.0) was added to the gel precursor mix (at 0.95 mM) to bind residual norbornene groups via UV-mediated thiol-ene chemistry. For 3D cell encapsulation, a cell suspension ($5x10^5$ cells/ mL) was added to the precursor solution and mixed before UV exposure. Matrigel (356237, Corning) was used at 100% w/v concentration (~ 10mg/mL).

Mechanical characterization

Rheology measurements were performed to calculate the elastic modulus (E) of pre-formed gels. Norbornene-modified alginate (2% w/v) hydrogels with different stiffness were cast by changing the DTT crosslinker concentration (0.01-1 mg/mL). After gel equilibration overnight in PBS, frequency sweep measurements were performed from 0.01 to 10 Hz at 1% shear strain with an 8 mm parallel plate (PP08, Anton Paar) using a rheometer (Physica MCR 301; Anton Paar),

while keeping the temperature at 25 °C with a Peltier cooling module. The initial E modulus was then calculated as follows: $E = 2G(1+\vartheta)$ and $G = \sqrt{G'^2 + G''^2}$ where G, G' and G'' are the shear, storage and loss moduli, respectively, and ϑ the Poisson's ratio with a value of 0.5 for hydrogels(*33*).

Cell culture

MDA-MB-231 (HTB-26; ATCC), MDA-MB-231-1883 BoM (provided by Dr. Joan Massagué and purchased from the Antibody and Bioresource Core Facility of the Memorial Sloan Kettering Cancer Center, USA. The subclone 1833 is a bone tropic human cell line deriving from a metastasis formed by MDA-MB-231 TGL cells hosted in a mouse(*34*, *35*),which in turn are MDA-MB-231 (HTB-26; ATCC) human epithelial breast cancer cells stably transduced with a lentivirus expressing a triple-fusion reporter(*36*)) and MCF-7 (HTB-22; ATCC) human breast cancer cell lines were cultured in low glucose Dulbecco's Modified Eagle's Medium (D6046; Sigma-Aldrich) with 10% v/v fetal bovine serum (S0615, Sigma-Aldrich) and 1% penicillin/streptomycin (Gibco). For MCF-7 cells, 0.1% insulin (I1882, Sigma-Aldrich) was added. Cells were then incubated in a 5% CO_2 environment at 37 °C and passaged every 3-5 days.

Viability and metabolic activity characterization

Live and dead cells were stained with 1.6 mM calcein AM (C125400; TRC) and 4 mM ethidium homodimer-1 (EthD-1 L3224; ThermoFisher), respectively. To measure metabolic activity, Presto blue (ThermoFisher) was used. Briefly, after 1 and 7 days of incubation, cell culture medium was replaced with 10% Presto blue reagent in DMEM and the plate incubated for at least 4 h at 37 °C. Next, 100 µL of the supernatant was transferred to a black 96 well plate (655892, Greiner Bio-one) and fluorescence emission was measured at 590 nm (Cytation5, BioTek). ATP concentration was measured using CellTiter-Glo (Promega) according to the manufacturer's instruction. Briefly, a 1:1 volume of reagent and culture medium was added to each sample of a black 96 well plate (655892, Greiner Bio-one), shaken for 10 min at room temperature, and allowed to equilibrate for another 20 min before measuring bioluminescence signal (Cytation5, BioTek).

Lentiviral particle production, transduction and generation of FUCCI2 breast cancer cell lines

As previously reported(*37*), FUCCI2 vectors mCherry hCdt1(30/120)/pCSII EF MCS (DDBJ/EMBL/GenBank, AB512478) and mVenus hGeminin(1/100)/pCSII EF MCS (DDBJ/EMBL/GenBank, AB512479) were purchased from the Riken Brain Science Institute (Japan) and used to generate lentivirus particles by co-transfecting HEK 293TN cells (System Biosciences) with packaging (psPAX2, Addgene plasmid, #12260) and envelope (pMD2.G (Addgene plasmid, #12259) plasmids. The supernatant was collected by centrifuging (Beckman L7-55 with SW32Ti rotor) at 22,000 rpm for 3h at 4 °C. MDA-MB-231 and MCF-7 breast cancer cell lines were first transfected with mVenus hGeminin (1/110) (multiplicity of infection (MOI) of six and five, respectively) followed by mCherry hCdt1 (30/120) at an MOI of three. Verification of successful transduction and subsequent sorting of stably expressing mVenus and mCherry cell lines were perform using flow cytometry (FACSAriaTM II, Becton Dickinson).

Inhibition, RNA interference and drug response experiments

For inhibition experiments, the following small molecule and inhibitors were used: MEK/ERK inhibitor PD98059 (10 mM, Focus Biomolecules), JNKinhibitor SP600125 (10 mM, Focus Biomolecules) and PI3K/Akt inhibitor LY294002 (10 mM, Focus Biomolecules). The inhibitors were mixed with culture medium and refreshed every 2-3 days. To knock down FHL2, MDA-MB-231 cells were transfected with two different FHL2-targeting small interfering RNAs (Silencer siRNA, Invitrogen) or non-targeting siRNA (Stealth RNAi negative control, Invitrogen) using Lipofectamine RNAiMAX Reagent (Invitrogen), diluted in Opti-MEM reduced serum

334 medium (Gibco) for a final concentration of 10-20 nM. Cells were transfected 2-3 days before
335 encapsulation following manufacturer's instructions. To assess MDA-MB-231 response to
336 chemotherapy, Paclitaxel (Tokyo Chemical Industry) was diluted at 0.01, 0.1 and 0.5 mM and
337 added to the culture medium after 3-5 days post-encapsulation for a drug treatment of 2 days. The
338 highest concentration tested contained around 1% (v/v) of DMSO, which was used as vehicle
339 medium and didn't show any negative effect on cell viability.

340 **Immunofluorescence staining**

341 Gels with encapsulated cells were washed (3x) with PBS and fixed with 4%
342 paraformaldehyde (PFA, Boster, #AR1068) for 30 min at room temperature, (3x) washed with 3%
343 w/v bovine serum albumin (BSA, Sigma Aldrich), permeabilized with 0.1 % w/v Triton X 100
344 (Sigma-Aldrich, #T8787) for 15 min with a final washing (3x) step with 3% BSA. Whole-mount
345 primary antibody staining was performed at 4 °C overnight, diluted in a 3% BSA+0.1% Triton X
346 100 buffer solution under mild shaking. The gels were then washed (3x) with 3% BSA and
347 incubated with secondary antibody at 4 °C overnight with the same dilution buffer under mild
348 shaking. The samples were finally imaged after a last washing step with PBS (3x). The primary
349 antibodies and respective concentrations used in this study are the following: anti-Ki67 (2 µg/mL,
350 ab15580, abcam), anti-p21$^{Cip1/Waf1}$ (0.48 µg/mL, 2947S, Cell Signaling), anti-FHL2 (0.5 µg/mL,
351 HPA006028, Sigma/Prestige Antibodies). The secondary antibodies are: Alexa Fluor 405 (10
352 µg/mL, ab175651, abcam) and Alexa Fluor 647 (4 µg/mL, A21244, Invitrogen). To stain for
353 nucleus and cytoskeleton, DAPI (1:1000, Roche) and Alexa Fluor 488 Phalloidin (1:50, Invitrogen)
354 were used.

355 **Immunoblot**

356 Cells were first lysed with RIPA buffer (Abcam) for 5 min on ice and then collected in
357 Eppendorf tubes. Protein concentration was calculated following Bradford assay (Bradford reagent,
358 Sigma-Aldrich). A 1:50 mixture of β-mercaptoethanol (Acros Organics) and 2x Tricine sample
359 buffer (Bio-Rad) was added at a 1:1 volume to the cell lysates. The mixture was then heated to
360 95 °C for 5 min and loaded into pre-cast polyacrylamide gels (Mini-PROTEAN TGX, Bio-Rad)
361 for electrophoresis in TGS buffer (Bio-Rad) at 100 V for 30 min, then 200 V for 30 min (Mini-
362 PROTEAN Tetra System, Bio-Rad). Proteins in the gels were then blotted onto to a PVDF
363 membrane (BioTrace, PALL) at 150 V for 90 min in ice-cold transfer buffer (1:5 volume of 100%
364 Methanol in TGS buffer). Next, the membrane was transferred to TBST buffer (150 mM NacL, 20
365 mM Tris-base, 0.1% Tween20), blocked in 5% BSA in TBST buffer for 1 h under gentle shaking,
366 washed in TBST (3x) and incubated with primary antibodies diluted in 1% BSA in TBST overnight
367 at 4 °C. After washing with TBST (3x), the membrane was incubated with an HRP-linked
368 secondary antibody for 1 h at room temperature, after which the chemoluminescence substrate
369 (SuperSignal West Pico PLUS, Thermo Scientific) was added before visualizing it with a blot
370 imager (G:BOX Chemi XX6/XX9, Syngene). GAPDH (1:1000, 2118, Cell Signaling) was used as
371 housekeeping gene and HRP-linked (1:1000, 7074, Cell Signaling) as secondary antibody.

372 **Cell retrieval from 3D gels**

373 For RNA sequencing, MDA-MB-231 cells were retrieved from 3D alginate stiff, soft and
374 3D Matrigel. Briefly, alginate hydrogels were incubated with alginate lyase (2mg/mL, Sigma
375 Aldrich, A1603) in HBSS (ThermoFisher, 14185045) for 30 min at 37 °C with three mixture steps
376 every 10 min. For Matrigel, pre-cooled (4°C) HBSS was added and mixed for 5-10 min at room
377 temperature, followed by incubation with Trypsin/EDTA (0.05%/0.02%, PAN Biotech, P10-
378 023100) for 5 min at 37 °C. Cells were then washed twice with HBSS for 5 min. Next, retrieved
379 cells were stained using a LIVE/DEAD fixable cell staining method (ThermoFisher, L34969)
380 following manufacturer's instructions, and viable cells were sorted via FACSAria II flow cytometer
381 (Becton Dickinson). Approximately 1500 sorted cells per sample were then lysed using pre-cooled

(4 °C) RLN buffer (0.05 M Tri-HCl pH 8.0, 0.14 M NaCl, 0.0015 M $MgCl_2$, 0.5 % v/v Nonidet P-40/IGEPAL (Sigma Aldrich, 56741) and 1000 U/mL RNase inhibitor (Promega, N2615), 0.001 M DTT) on ice for 5 min. The lysates were then centrifuged with a pre-cooled centrifuge for 2 min at 300 x g, the supernatants transferred to -80 °C and stored until further processing.

RNA sequencing and analysis

Samples were resuspended in 5 µl 1X NEBNext Cell Lysis Buffer of the NEBNext Single Cell/Low Input RNA Library Prep Kit (NEB, E6420). After 5 min incubation at RT, 2.5X RNA XP Clean Up Beads (Beckman Coulter, A63987) were added to the sample by pipetting up and down. Then, samples were incubated for 5 min at RT, the beads were pelleted on a magnet, the supernatant was removed, the samples were washed twice with 80% ethanol while remaining on the magnet, and finally the beads were resuspended in 8 µl nuclease-free water. The reverse transcription was conducted according to the manual of the NEBNext Single Cell/Low Input RNA Library Prep Kit in the presence of the beads. Next, the beads were pelleted on the magnet and the supernatant was used for the following PCR amplification as described in the manual. Twenty-one PCR cycles were applied, because the RNA concentration was below the detection limit of the Qubit RNA HS Assay Kit (Thermo Fisher, Q23852). The cleanup, quality control, fragmentation, and adapter ligation steps were performed as described in the kit manual. NEBNext Multiplex Oligos for Illumina (Index Primer Set 1) (NEB, 7335S) were used for the final PCR amplification. The fragment length distribution of the final libraries was determined using a 2100 Bioanalyzer Instrument (Agilent) with a High Sensitivity DNA kit (Agilent, 5067-4626). The libraries were quantified by qPCR with the KAPA Library Quantification Kit (Roche, KK4854). The nine samples were divided into two pools (one pool of four samples, the other of five samples) with equimolar amount. The pools were sequenced on an Illumina MiSeq with 2 x 150 bp.

After demultiplexing, raw FASTQ data were given to an in-house mRNA analysis pipeline 0.9.5.5. BBDuk 38.76(*38*) was used to trim the raw sequence data from soft, 3D matrigel and 3D alginate stiff, deleting any residual adapter sequences and low-quality bases at the ends of each read. BioBloom Tools 2.0.13(*39*) was used to decontaminate reads from the genomes Mus musculus (mm38), Escherichia coli (BL21), Mycoplasma pneumoniae (M129), Sphingobium sp. (SYK-6), Bradyrhizobium japonicum (USDA 110), Pichia pastoris (GS115), Malessia globosa (CBS 7966), Aspergillus fumigatus (Af293), and a set of viral genomes (RefSeq, 5k+ genomes). All reads that did not map exclusively to the transcriptome of hg38 (GENCODE version 27, GRCh38.p10) were labeled as potentially contaminated and were removed from further processing. FastQC 0.11.9(*40*) was used to evaluate sequence quality per sample before as well as after trimming and decontamination. In addition, all samples were examined as a collective with MultiQC 1.8(*41*). Following that, the cleaned sample reads were aligned to the hg38 reference genome using STAR 2.5.1b(*42*). Using featureCounts from Subread 2.0.0, uniquely mapping reads were counted per gene and sample(*43*). Further quality criteria were evaluated, including library complexity (using Preseq 2.0.3(*44*)) and the genomic origin of the reads and the 5'-3'-bias (both using QualiMap 2.2.2d(*45*)). The final counts table of 9 samples were utilized for differential expression analysis.

All the subsequent steps after the count tables were performed in R programming language 4.0.2 (2020-06-22)(*46*). Matrix table containing gene counts were visualized using Principle Component Analysis (PCA) and t-distributed stochastic neighbor embedding (t-SNE) clustering techniques. For PCA, raw counts were scaled and prcomp function from stats package was employed. tSNE plots were constructed using Rtsne 0.15(*47*). Subsequent steps including Quality Control (QC) analysis, filtering, normalization, feature selection, scaling, regression of unwanted variables were performed using Seurat package 4.0.2(*48*). Default parameters were taken for all used functions unless otherwise mentioned. Normalization was done using 'log.normalize' method with a scale factor of $1x10^{-6}$ to obtain logCPM count values and 2,000 most variable genes were

used for feature selection. Only mitochondrial genes were regressed out during scaling, cell cycle associated genes did not have an effect on the cell-to-cell clustering. "DESeq2" method was applied to do differential expression analysis between the three groups, soft, stiff and matrigel and in addition testing of genes was limited to a logFoldChange (logFC) cutoff of 1. Further, the differentially expressed genes were manually filtered for an adjusted *p-value* of 0.05. Finally, volcano plots were constructed using EnhancedVolcano 1.8.0(*49*). In addition to applying single cell method, Seurat, we also applied pure bulk RNA seq method, DESeq2(*50*), to perform the data analysis of the single cell pool samples. Results from both methods were highly similar including the list of differentially expressed genes, their respective fold changes and adjusted *p*-value. We chose to report results from Seurat due to the zero-inflated count distribution of our data which is typical of single cells than bulk RNA data (Supp.Fig.4).

Gene Set Enrichment Analysis (GSEA) of significantly Differentially Expressed Genes (DEGs) (adjusted p-value < 0.05 and $|\text{logFC}| > 1$) into functional categories were performed using Bioconductor packages 1.30.15. GOseq 1.42.0(*51*) and clusterProfiler 3.18.1(*52*) were used, respectively, to conduct Gene Ontology (GO)(*53*) and Kyoto Encyclopedia of Genes and Genomes (KEGG)(*54*) enrichment analyses. All the enrichment plots including GSEA, dot plot and heatmap were made using built-in functions in Seurat package or ggplot2 3.3.3(*55*). Network maps were processed based on the selected enriched GO categories using Cytoscape 3.8.2 and enrichment Map plugin(*56*).

Animal experiment

12-week-old female BALB/c nude mice (CAnN.Cg-Foxn1nu/Crl, Charles River, Sulzfeld, Germany) were acclimatized in the animal facility of the Charité-Universitätsmedizin Berlin and housed with ad libitum access to food and water. Mice injected into the left ventricle of the heart with MDA-MB-231-1833 BoM cells ($5x10^5$ cells in 100 µL ice cold PBS), using a 27G needle, under ultrasound guidance (Vevo2100, FUJIFILM VisualSonics Inc., Canada). The animals received Carprosol (CP-Pharma Handelsgesellschaft mbH, Burgdorf, Germany) and Bupresol (CP-Pharma Handelsgesellschaft mbH, Burgdorf, Germany) as analgesic drugs during and after the injection. The animals were anesthetized using isoflurane (CP-Pharma Handelsgesellschaft mbH, Burgdorf, Germany) and the eyes were protected from drying with Pan-Ophtal gel (Dr. Winzer Pharma GmbH, Berlin, Germany). The mouse was sacrificed after 2 weeks by cervical dislocation. The hind limbs were harvested and fixed with 4% paraformaldehyde (PFA) in phosphate-buffered saline (PBS) for 12 h at 4 °C and stored in PBS until further processing. All animal experiments were carried out according to the policies and procedures approved by local legal research animal welfare representatives (LAGeSo Berlin, G0224/18).

For each mouse, bones of one limb were cold embedded at 4°C in poly(methyl methacrylate) (PMMA) (Technovit 9100, Kulzer, Germany), following the manufacturer's instructions. Briefly, samples were dehydrated in an ascending ethanol series, followed by a xylene washing step, infiltration and embedding in PMMA. The staining was performed on 6 µm thick longitudinal sections using a standard protocol of Haematoxylin and Eosin staining (H & E Rapid kit, Clin-Tech, Surrey, UK). Samples were washed in tap water, followed by staining in Carazzi's double-strength Haematoxylin. After another wash in tap water, the slides were stained in Eosin, rinsed in tap water, dehydrated and mounted. The stained sections were imaged with a Keyence Digital Microscope (VKX-5550E, Keyence, Germany). For immunostaining of the slides, after deplastification and rehydration, antigen retrieval was performed (sodium citrate pH 6.0/ 0.05% Tween20) at 105°C for 15 min, followed by 10 min quenching of endogenous peroxidase activity with 3% hydrogen peroxide (Sigma-Aldrich), and a final blocking was performed with Background Sniper (Biocare Medical, Concord, CA, USA) for 10 min. Primary (FHL2 2 µg/mL and Ki67 2 µg/mL) and secondary antibodies (same as for in vitro immunofluorescence staining) were diluted in Dako antibody diluent (Dako, Germany). Washing steps were done in Dako washing buffer.

480 Slides were then mounted with Vectashield antifade mounting medium (Biozol, Germany)
481 following manufacturer's instructions.

482 Bones of the other limb of the mouse were freeze embedded following the method of the
483 SECTION-LAB Co. Ltd. (Hiroshima, Japan). The samples were dehydrated in an ascending
484 sucrose solution (10%, 20% and 30% in distilled water) for 24 h each at 4°C. Following this, a
485 metal mold was placed in cooled isopropanol and filled with embedding medium (SCEM;
486 SECTION-LAB Co. Ltd.), placing the bone in the middle. Cryosections with a thickness of 20 µm
487 were cut following the Kawamoto method(*57*) using a cryostat (Leica CM3060S). The section was
488 collected using a Kawamoto film (cryofilm type II C(9)) and later attached to a microscopic slide
489 and stored at -20°C until further use. For immunostaining the slides were blocked with blocking
490 buffer (1%BSA/ 0.1%Tween20 in PBS). Primary and secondary antibodies were diluted in blocking
491 buffer and incubated for at least 4 and 1h at room temperature, respectively. Washing steps (2x for
492 15min) were conducted in washing buffer (0.1%Tween20 in PBS) and distilled water. Slides were
493 then mounted with Dako fluorescence mounting media (S302380-2, Agilent Technologies).

494 **Immunofluorescence staining of human early DCCs in lymph node samples of an M0 breast**
495 **cancer patient**

496 After informed consent (ethics vote number 18-948-101), the sentinel lymph node of an
497 M0-stage breast cancer patient (i.e. with no evidence of distant metastasis) was first divided into
498 two halves and one half examined by histopathology. The other half was disaggregated
499 mechanically (DAKO Medimachine, DAKO) to generate a single-cell suspension. Then,
500 mononuclear cells were isolated using a density gradient centrifugation (60% Percoll solution,
501 Amersham) and plated onto adhesive slides. After sedimentation of the cells, the supernatant was
502 discarded and slides were air-dried and stored at -20°C. For immunofluorescence staining of FHL2
503 and Cytokeratin 8/18/19, the slides were first thawed at RT and moistened with PBS. Cells were
504 fixed with 2% PFA (Sigma, P6148) for 10 min, washed twice with PBS and permeablized with
505 0.05% TritonX100 for 5 min. After two additional washing steps with PBS, cells were blocked with
506 PBS/10% AB serum (#805135, Bio-Rad) for 1.5 hours at RT. Primary antibody incubation with
507 monoclonal mouse anti-human Cytokeratin 8/18/19 (2 µg/mL, clone A45-B/B3, AS Diagnostik)
508 and polyclonal rabbit anti-human FHL2 (2 µg/mL, HPA006028, Sigma/Prestige Antibodies) was
509 performed at 4 °C overnight in PBS/10% AB serum. Following washing with PBS (4x 20 min), the
510 slides were incubated with secondary antibodies, anti-mouse AlexaFluor 488 (5 µg/mL, A11029,
511 Invitrogen) and anti-rabbit AlexaFluor Plus 647 (5 µg/mL, A32733, Invitrogen) and DAPI
512 (1µg/mL, MBD0015, Sigma) in PBS/5% AB serum/2.5% goat serum for 1.5 hours. After washing
513 off the secondary antibodies (PBS 3x 10 min) the slides were mounted with SlowFade™ Glass
514 Soft-set Antifade Mountant (S36917, Invitrogen) and imaged on Zeiss LSM980. Images were
515 processed with ImageJ (v.1.53q) to show the max-z-projections.

516 **Image acquisition and analysis**

517 Live-cell imaging was conducted in a stage top incubator (Okolab, UNO-T-H-CO_2)
518 mounted on an inverted epifluorescence microscope (Zeiss, AxioObserver 7) and a 10x, 0.3 NA
519 objective at 37 °C and 5% CO_2. Images were recorded every 6 h for 4-5 days. For FUCCI2 image
520 analysis, live-cell imaging of cells on 2D TCP or 3D hydrogels was performed and mCherry and
521 mVenus fluorescence signals were recorded every 6 h. Briefly, after choosing a focus plane at the
522 beginning of the experiment for each field of view, a z-stack of this region/20 µm was acquired
523 around this position, and phase contrast as well as fluorescence images were recorded.

524 At the end of the experiment, *in situ* viability staining with calcein was performed and the
525 same z-stack/middle-focus plain as the final timelapse acquisition step was acquired. This allowed
526 longitudinal correlation of viability at the end of the experiment with cell cycle progression over
527 the course of the experiment. The number of cdt1- cells at the final timepoint was counted as the

difference between FUCCI2+ cells (cells that either express mCherry or mVenus) at the initial and the last timepoint, with additional reference to phase contrast images. Next, viable (calcein+) single cells were counted and the dynamics of their FUCCI2 fluorescence signal extracted using a semi-automated custom-made MATLAB script. To do this, viable cells were picked and tracked over and mean nuclear FUCCI2 intensity was extracted.

To quantify viability, projected images were thresholded for each channel corresponding to viable (calcein +) or dead (EthD-1) cells using a counting custom-made MATLAB script. To quantify immunofluorescence, images were first thresholded for nucleus (DAPI) and cytoskeleton (F-Actin) to localize single cells, after which the immunofluorescence signal intensity within the defined boundaries was extracted for each cell. The background signal of negatively-stained samples was used to define the threshold for positive cells. The described process was performed using an automated custom-made MATLAB script.

To quantify p21 and FHL2 localization, a Leica SP8 confocal microscope with 63x, 1.4 NA oil-immersion objective was used. Briefly, images were thresholded for nucleus (DAPI) and cytoskeleton (F-Actin) to define the respective intracellular regions, after which p21 or FHL2 average intensity within each region was recorded. The described process was performed using an automated custom-made MATLAB script.

Images of human tissue samples from patients with primary breast cancer were obtained from the Human Protein Atlas (www.proteinatlas.org)(*58*). Samples with strong FHL2 intensity were selected, of which the localization was already designated as being either nuclear or cytoplasmic.

Statistical analysis

For statistical comparison between two groups, two-tailed student's t-test or Mann-Whitney U-test were performed for normally-distributed or non-parametric groups, respectively (*: $p \leq 0.05$, **: $p \leq 0.01$, ***: $p \leq 0.001$, ****: $p \leq 0.0001$). One-way Anova with Tukey's correction or Kruskal-Wallis test with Dunn's correction were conducted for multiple-group comparison. Error bars indicate mean and standard deviation used for fraction graphs. Datasets shown as box plots with median, for 25th to 75th percentiles and whiskers for minimum and maximum used for ratio graphs. Violin plots show dashed lines for median and dotted lines for the two quartile lines, used for fluorescence intensity graphs. GraphPad Prism 8 software was used to plot the data and for statistical analysis.

References

1. C. A. Klein, Cancer progression and the invisible phase of metastatic colonization. *Nat. Rev. Cancer*. **20**, 681–694 (2020).
2. C. M. Ghajar, Metastasis prevention by targeting the dormant niche. *Nat. Rev. Cancer*. **15**, 238–247 (2015).
3. M. Montagner, E. Sahai, In vitro Models of Breast Cancer Metastatic Dormancy. *Front. Cell Dev. Biol.* **8**, 1–10 (2020).
4. S. Galarza, A. J. Crosby, C. Pak, S. R. Peyton, Control of Astrocyte Quiescence and Activation in a Synthetic Brain Hydrogel. *Adv. Healthc. Mater.* **9**, 1901419 (2020).
5. M. Quarta, J. O. Brett, R. DiMarco, A. De Morree, S. C. Boutet, R. Chacon, M. C. Gibbons, V. A. Garcia, J. Su, J. B. Shrager, S. Heilshorn, T. A. Rando, An artificial niche preserves the quiescence of muscle stem cells and enhances their therapeutic efficacy. *Nat. Biotechnol.* **34**, 752–759 (2016).

576 6. C. M. Madl, B. L. LeSavage, R. E. Dewi, C. B. Dinh, R. S. Stowers, M. Khariton, K. J.
577 Lampe, D. Nguyen, O. Chaudhuri, A. Enejder, S. C. Heilshorn, Maintenance of neural
578 progenitor cell stemness in 3D hydrogels requires matrix remodelling. *Nat. Mater.* **16**, 1233–
579 1242 (2017).
580 7. A. Roch, S. Giger, M. Girotra, V. Campos, N. Vannini, O. Naveiras, S. Gobaa, M. P. Lutolf,
581 Single-cell analyses identify bioengineered niches for enhanced maintenance of
582 hematopoietic stem cells. *Nat. Commun.* **8**, 221 (2017).
583 8. C. Yang, M. W. Tibbitt, L. Basta, K. S. Anseth, Mechanical memory and dosing influence
584 stem cell fate. *Nat. Mater.* **13**, 645–652 (2014).
585 9. S. Khetan, M. Guvendiren, W. R. Legant, D. M. Cohen, C. S. Chen, J. A. Burdick,
586 Degradation-mediated cellular traction directs stem cell fate in covalently crosslinked three-
587 dimensional hydrogels. *Nat. Mater.* **12**, 458–465 (2013).
588 10. S. Pradhan, J. H. Slater, Tunable hydrogels for controlling phenotypic cancer cell states to
589 model breast cancer dormancy and reactivation. *Biomaterials*. **215**, 119177 (2019).
590 11. S. Nam, V. K. Gupta, H. Lee, J. Y. Lee, K. M. Wisdom, S. Varma, E. M. Flaum, C. Davis,
591 R. B. West, O. Chaudhuri, Cell cycle progression in confining microenvironments is
592 regulated by a growth-responsive TRPV4-PI3K/Akt-p27 Kip1 signaling axis. *Sci. Adv.* **5**,
593 eaaw6171 (2019).
594 12. O. Chaudhuri, S. T. Koshy, C. Branco da Cunha, J.-W. Shin, C. S. Verbeke, K. H. Allison,
595 D. J. Mooney, Extracellular matrix stiffness and composition jointly regulate the induction
596 of malignant phenotypes in mammary epithelium. *Nat. Mater.* **13**, 970–978 (2014).
597 13. B. R. Seo, P. Bhardwaj, S. Choi, J. Gonzalez, R. C. Andresen Eguiluz, K. Wang, S. Mohanan,
598 P. G. Morris, B. Du, X. K. Zhou, L. T. Vahdat, A. Verma, O. Elemento, C. A. Hudis, R. M.
599 Williams, D. Gourdon, A. J. Dannenberg, C. Fischbach, Obesity-dependent changes in
600 interstitial ECM mechanics promote breast tumorigenesis. *Sci. Transl. Med.* **7**, 301ra130-
601 301ra130 (2015).
602 14. A. Lueckgen, D. S. Garske, A. Ellinghaus, D. J. Mooney, G. N. Duda, A. Cipitria,
603 Enzymatically-degradable alginate hydrogels promote cell spreading and in vivo tissue
604 infiltration. *Biomaterials*. **217**, 119294 (2019).
605 15. A. Sakaue-Sawano, H. Kurokawa, T. Morimura, A. Hanyu, H. Hama, H. Osawa, S.
606 Kashiwagi, K. Fukami, T. Miyata, H. Miyoshi, T. Imamura, M. Ogawa, H. Masai, A.
607 Miyawaki, Visualizing Spatiotemporal Dynamics of Multicellular Cell-Cycle Progression.
608 *Cell*. **132**, 487–498 (2008).
609 16. A. Sakaue-Sawano, T. Kobayashi, K. Ohtawa, A. Miyawaki, Drug-induced cell cycle
610 modulation leading to cell-cycle arrest, nuclear mis-segregation, or endoreplication. *BMC*
611 *Cell Biol.* **12**, 2 (2011).
612 17. S. Gookin, M. Min, H. Phadke, M. Chung, J. Moser, I. Miller, D. Carter, S. L. Spencer, A
613 map of protein dynamics during cell-cycle progression and cell-cycle exit. *PLOS Biol.* **15**,
614 e2003268 (2017).
615 18. A. Karimian, Y. Ahmadi, B. Yousefi, Multiple functions of p21 in cell cycle, apoptosis and
616 transcriptional regulation after DNA damage. *DNA Repair (Amst).* **42**, 63–71 (2016).
617 19. B. M. Baker, C. S. Chen, Deconstructing the third dimension – how 3D culture
618 microenvironments alter cellular cues. *J. Cell Sci.* **125**, 3015–3024 (2012).
619 20. B. T. Martin, K. Kleiber, V. Wixler, M. Raab, B. Zimmer, M. Kaufmann, K. Strebhardt,
620 FHL2 Regulates Cell Cycle-Dependent and Doxorubicin-Induced p21Cip1/Waf1
621 Expression in Breast Cancer Cells. *Cell Cycle*. **6**, 1779–1788 (2007).
622 21. N. Nakazawa, A. R. Sathe, G. V. Shivashankar, M. P. Sheetz, Matrix mechanics controls
623 FHL2 movement to the nucleus to activate p21 expression. *Proc. Natl. Acad. Sci.* **113**,
624 E6813–E6822 (2016).
625 22. J. Y. Lee, J. K. Chang, A. A. Dominguez, H. Lee, S. Nam, J. Chang, S. Varma, L. S. Qi, R.

B. West, O. Chaudhuri, YAP-independent mechanotransduction drives breast cancer progression. *Nat. Commun.* **10**, 1848 (2019).

23. O. Y. Dudaryeva, A. Bucciarelli, G. Bovone, F. Huwyler, S. Jaydev, N. Broguiere, M. Al-Bayati, M. Lütolf, M. W. Tibbitt, 3D Confinement Regulates Cell Life and Death. *Adv. Funct. Mater.* **i**, 2104098 (2021).
24. K. Kleiber, K. Strebhardt, B. T. Martin, The biological relevance of FHL2 in tumour cells and its role as a putative cancer target. *Anticancer Res.* **27**, 55–62 (2007).
25. J. Albrengues, M. A. Shields, D. Ng, C. G. Park, A. Ambrico, M. E. Poindexter, P. Upadhyay, D. L. Uyeminami, A. Pommier, V. Küttner, E. Bružas, L. Maiorino, C. Bautista, E. M. Carmona, P. A. Gimotty, D. T. Fearon, K. Chang, S. K. Lyons, K. E. Pinkerton, L. C. Trotman, M. S. Goldberg, J. T. H. Yeh, M. Egeblad, Neutrophil extracellular traps produced during inflammation awaken dormant cancer cells in mice. *Science (80-.).* **361**, eaao4227 (2018).
26. D. Barkan, H. Kleinman, J. L. Simmons, H. Asmussen, A. K. Kamaraju, M. J. Hoenorhoff, Z. -y. Liu, S. V. Costes, E. H. Cho, S. Lockett, C. Khanna, A. F. Chambers, J. E. Green, Inhibition of Metastatic Outgrowth from Single Dormant Tumor Cells by Targeting the Cytoskeleton. *Cancer Res.* **68**, 6241–6250 (2008).
27. J. A. Aguirre Ghiso, Inhibition of FAK signaling activated by urokinase receptor induces dormancy in human carcinoma cells in vivo. *Oncogene*. **21**, 2513–2524 (2002).
28. T. Shibue, R. A. Weinberg, Integrin 1-focal adhesion kinase signaling directs the proliferation of metastatic cancer cells disseminated in the lungs. *Proc. Natl. Acad. Sci.* **106**, 10290–10295 (2009).
29. E. E. Er, M. Valiente, K. Ganesh, Y. Zou, S. Agrawal, J. Hu, B. Griscom, M. Rosenblum, A. Boire, E. Brogi, F. G. Giancotti, M. Schachner, S. Malladi, J. Massagué, Pericyte-like spreading by disseminated cancer cells activates YAP and MRTF for metastatic colonization. *Nat. Cell Biol.* **20**, 966–978 (2018).
30. M. Werner-Klein, A. Grujovic, C. Irlbeck, M. Obradović, M. Hoffmann, H. Koerkel-Qu, X. Lu, S. Treitschke, C. Köstler, C. Botteron, K. Weidele, C. Werno, B. Polzer, S. Kirsch, M. Gužvić, J. Warfsmann, K. Honarnejad, Z. Czyz, G. Feliciello, I. Blochberger, S. Grunewald, E. Schneider, G. Haunschild, N. Patwary, S. Guetter, S. Huber, B. Rack, N. Harbeck, S. Buchholz, P. Rümmele, N. Heine, S. Rose-John, C. A. Klein, Interleukin-6 trans-signaling is a candidate mechanism to drive progression of human DCCs during clinical latency. *Nat. Commun.* **11**, 4977 (2020).
31. B. Gabriel, D.-C. Fischer, M. Orlowska-Volk, A. zur Hausen, R. Schüle, J. M. Müller, A. Hasenburg, Expression of the Transcriptional Coregulator FHL2 in Human Breast Cancer: A Clinicopathologic Study. *J. Soc. Gynecol. Investig.* **13**, 69–75 (2006).
32. A. Lueckgen, D. S. Garske, A. Ellinghaus, D. J. Mooney, G. N. Duda, A. Cipitria, Enzymatically-degradable alginate hydrogels promote cell spreading and in vivo tissue infiltration. *Biomaterials*. **217**, 119294 (2019).
33. S. T. Gould, N. J. Darling, K. S. Anseth, Small peptide functionalized thiol–ene hydrogels as culture substrates for understanding valvular interstitial cell activation and de novo tissue deposition. *Acta Biomater.* **8**, 3201–3209 (2012).
34. A. J. Minn, G. P. Gupta, P. M. Siegel, P. D. Bos, W. Shu, D. D. Giri, A. Viale, A. B. Olshen, W. L. Gerald, J. Massagué, Genes that mediate breast cancer metastasis to lung. *Nature*. **436**, 518–524 (2005).
35. Y. Kang, P. M. Siegel, W. Shu, M. Drobnjak, S. M. Kakonen, C. Cordón-Cardo, T. A. Guise, J. Massagué, A multigenic program mediating breast cancer metastasis to bone. *Cancer Cell*. **3**, 537–549 (2003).
36. V. Ponomarev, M. Doubrovin, I. Serganova, J. Vider, A. Shavrin, T. Beresten, A. Ivanova, L. Ageyeva, V. Tourkova, J. Balatoni, W. Bornmann, R. Blasberg, J. Gelovani Tjuvajev, A

novel triple-modality reporter gene for whole-body fluorescent, bioluminescent, and nuclear noninvasive imaging. *Eur. J. Nucl. Med. Mol. Imaging*. **31**, 740–751 (2004).
37. H. M. Taïeb, D. S. Garske, J. Contzen, M. Gossen, L. Bertinetti, T. Robinson, A. Cipitria, Osmotic pressure modulates single cell cycle dynamics inducing reversible growth arrest and reactivation of human metastatic cells. *Sci. Rep.* **11**, 13455 (2021).
38. BBtools software suite. *JGI DataScience* (2019).
39. J. Chu, S. Sadeghi, A. Raymond, S. D. Jackman, K. M. Nip, R. Mar, H. Mohamadi, Y. S. Butterfield, A. G. Robertson, I. Birol, BioBloom tools: fast, accurate and memory-efficient host species sequence screening using bloom filters. *Bioinformatics*. **30**, 3402–3404 (2014).
40. S. Andrews, FastQC: A Quality Control Tool for High Throughput Sequence Data. (2010).
41. P. Ewels, M. Magnusson, S. Lundin, M. Käller, MultiQC: summarize analysis results for multiple tools and samples in a single report. *Bioinformatics*. **32**, 3047–3048 (2016).
42. A. Dobin, C. A. Davis, F. Schlesinger, J. Drenkow, C. Zaleski, S. Jha, P. Batut, M. Chaisson, T. R. Gingeras, STAR: ultrafast universal RNA-seq aligner. *Bioinformatics*. **29**, 15–21 (2013).
43. Y. Liao, G. K. Smyth, W. Shi, The Subread aligner: fast, accurate and scalable read mapping by seed-and-vote. *Nucleic Acids Res.* **41**, e108–e108 (2013).
44. C. Deng, T. Daley, A. Smith, Applications of species accumulation curves in large-scale biological data analysis. *Quant. Biol.* **3**, 135–144 (2015).
45. K. Okonechnikov, A. Conesa, F. García-Alcalde, Qualimap 2: advanced multi-sample quality control for high-throughput sequencing data. *Bioinformatics*. **32**, btv566 (2015).
46. R. C. Team, R: A Language and Environment for Statistical Computing. (2020).
47. L. van der Maaten, Accelerating t-SNE using Tree-Based Algorithms. *J. Mach. Learn. Res.* **15**, 3221–3245 (2014).
48. Y. Hao, S. Hao, E. Andersen-Nissen, W. M. Mauck, S. Zheng, A. Butler, M. J. Lee, A. J. Wilk, C. Darby, M. Zager, P. Hoffman, M. Stoeckius, E. Papalexi, E. P. Mimitou, J. Jain, A. Srivastava, T. Stuart, L. M. Fleming, B. Yeung, A. J. Rogers, J. M. McElrath, C. A. Blish, R. Gottardo, P. Smibert, R. Satija, Integrated analysis of multimodal single-cell data. *Cell*. **184**, 3573-3587.e29 (2021).
49. K. Blighe, S. Rana, M. Lewis, EnhancedVolcano: Publication-ready volcano plots with enhanced colouring and labeling. (2018).
50. M. I. Love, W. Huber, S. Anders, Moderated estimation of fold change and dispersion for RNA-seq data with DESeq2. *Genome Biol.* **15**, 550 (2014).
51. M. D. Young, M. J. Wakefield, G. K. Smyth, A. Oshlack, Gene ontology analysis for RNA-seq: accounting for selection bias. *Genome Biol.* **11**, R14 (2010).
52. G. Yu, L.-G. Wang, Y. Han, Q.-Y. He, clusterProfiler: an R Package for Comparing Biological Themes Among Gene Clusters. *Omi. A J. Integr. Biol.* **16**, 284–287 (2012).
53. M. Ashburner, C. A. Ball, J. A. Blake, D. Botstein, H. Butler, J. M. Cherry, A. P. Davis, K. Dolinski, S. S. Dwight, J. T. Eppig, M. A. Harris, D. P. Hill, L. Issel-Tarver, A. Kasarskis, S. Lewis, J. C. Matese, J. E. Richardson, M. Ringwald, G. M. Rubin, G. Sherlock, Gene Ontology: tool for the unification of biology. *Nat. Genet.* **25**, 25–29 (2000).
54. M. Kanehisa, S. Goto, M. Furumichi, M. Tanabe, M. Hirakawa, KEGG for representation and analysis of molecular networks involving diseases and drugs. *Nucleic Acids Res.* **38**, D355–D360 (2010).
55. H. Wickham, *ggplot2: Elegant Graphics for Data Analysis* (Springer-Verlag New York, 2016).
56. D. Merico, R. Isserlin, O. Stueker, A. Emili, G. D. Bader, Enrichment Map: A Network-Based Method for Gene-Set Enrichment Visualization and Interpretation. *PLoS One*. **5**, e13984 (2010).
57. T. Kawamoto, Use of a new adhesive film for the preparation of multi-purpose fresh-frozen

726 sections from hard tissues, whole-animals, insects and plants. *Arch. Histol. Cytol.* **66**, 123–
727 143 (2003).
728 58. M. Uhlen, C. Zhang, S. Lee, E. Sjöstedt, L. Fagerberg, G. Bidkhori, R. Benfeitas, M. Arif,
729 Z. Liu, F. Edfors, K. Sanli, K. von Feilitzen, P. Oksvold, E. Lundberg, S. Hober, P. Nilsson,
730 J. Mattsson, J. M. Schwenk, H. Brunnström, B. Glimelius, T. Sjöblom, P.-H. Edqvist, D.
731 Djureinovic, P. Micke, C. Lindskog, A. Mardinoglu, F. Ponten, A pathology atlas of the
732 human cancer transcriptome. *Science (80-.).* **357**, eaan2507 (2017).

733 59. Cortazar, A. R. *et al.* CANCERTOOL: A Visualization and Representation Interface to
734 Exploit Cancer Datasets. *Cancer Res.* **78**, 6320–6328 (2018).

735 60. Chen, F., Chandrashekar, D. S., Varambally, S. & Creighton, C. J. Pan-cancer molecular
736 subtypes revealed by mass-spectrometry-based proteomic characterization of more than 500
737 human cancers. *Nat. Commun.* **10**, 5679 (2019).

738 61. Chandrashekar, D. S. *et al.* UALCAN: An update to the integrated cancer data analysis
739 platform. *Neoplasia* **25**, 18–27 (2022).

740 62. Chandrashekar, D. S. *et al.* UALCAN: A Portal for Facilitating Tumor Subgroup Gene
741 Expression and Survival Analyses. *Neoplasia* **19**, 649–658 (2017).

742 63. Lánczky, A. & Győrffy, B. Web-Based Survival Analysis Tool Tailored for Medical
743 Research (KMplot): Development and Implementation. *J. Med. Internet Res.* **23**, e27633
744 (2021).

745 64. Győrffy, B. Survival analysis across the entire transcriptome identifies biomarkers with the
746 highest prognostic power in breast cancer. *Comput. Struct. Biotechnol. J.* **19**, 4101–4109
747 (2021).
748
749

750 **Acknowledgments**

751 This work was funded by the Deutsche Forschungsgemeinschaft (DFG) Emmy Noether grant (CI
752 203/2-1 to A. C., S. B, D.S. G, and S. A. E. Y.). A. C. also thanks the funding from IKERBASQUE
753 Basque Foundation for Science and from the Spanish Ministry of Science and Innovation
754 (PID2021-123013OB-I00). H. M. T. thanks the International Max Planck Research School
755 (IMPRS) on Multiscale Bio Systems for financial support. J.C. and M.G thank the support provided
756 by the Helmholtz Association through program-oriented funding and by the Federal Ministry of
757 Education and Research, Germany, as part of the program Health Research (BCRT; Grant No.
758 13GW0098). This work was funded by the Bavarian ministry of economic affairs, energy and
759 technology ("Aufbau einer Infrastruktur und Logistik zur translationalen Forschung mit Geweben
760 von Krebspatienten", AZ 20-3410.1-1-1). The authors thank the technicians of the Research
761 Workshop at the Charité-Universitätsmedizin Berlin for developing and manufacturing some
762 experimental devices. We thank the lab of Dr. Joan Massagué at the Memorial Sloan Kettering
763 Cancer Center, USA, for providing the MDA-MB-231-1883 BoM cells. We thank Aline Lueckgen,
764 Christine Pilz, Inés Moreno-Jiménez, Geonho Song, Tina Seeman, Nicky Tam, Reynel Urrea
765 Castellanos, Stefanie Güldener and Reinhild Dünnebacke for technical assistance with hydrogel
766 preparation, cell culture, immunostaining, rheology, confocal microscopy, immunoblotting, blot
767 imaging, RNA sequencing and microplate-reader measurements, respectively. The authors would
768 like to acknowledge Peter Fratzl, Maria M. Caffarel and Andrea Abaurrea for scientific discussion.
769

770 **Competing interests:** CAK is member of the SAB of HiberCell.

771

Figures

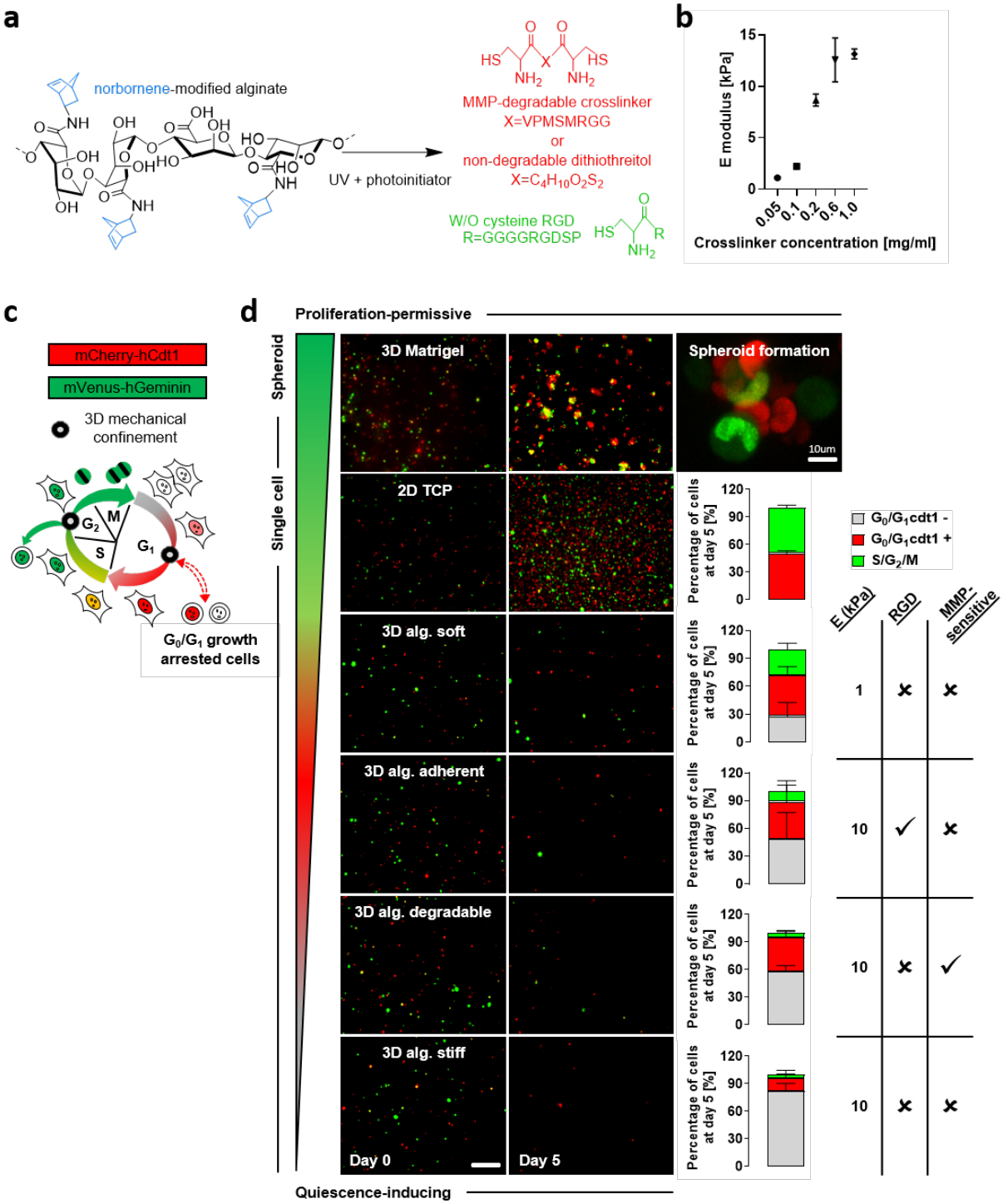

Fig. 1 3D mechanical confinement via covalently-crosslinked alginate yields distinct fractions and populations of growth-arrested cells based on hydrogel composition. a) Bis-cysteine enzymatically (MMP) degradable peptide or non-degradable dithiothreitol (DTT) (red) crosslink with norbornene-modified alginate (blue) in the presence or absence of cysteine-coupled RGD molecules (green). **b)** Frequency sweep of norbornene-modified alginate (no RGD) with different concentrations of DTT crosslinker yields a range of stiffness (Elastic/Young's moduli) (n=3). **c)** Diagram of FUCCI2 cell cycle reporter activity

(G_0/G_1=mCherry-hCdt1 and $S/G_2/M$=mVenus-hGeminin). The cartoon was adapted from Sakaue-Sawano et al.[15], Copyright (2008), with permission from Elsevier. **d)** Time lapse imaging (5 days) of MDA-FUCCI2 cells within a range of proliferation-permissive and quiescence-inducing hydrogels with distinct stiffness, adhesion and degradation properties (right-hand side table). Representative time lapse fluorescence maximum projections at day 0 and day 5, scale bar equals 200 μm. Scale bar equals 10 μm for 3D Matrigel spheroid image. Percentage bar plots show fraction of cell cycle distribution at day 5 for different experimental groups. Error bars indicate mean and standard deviation ($n \geq 3$ gels for 82 to 453 cells).

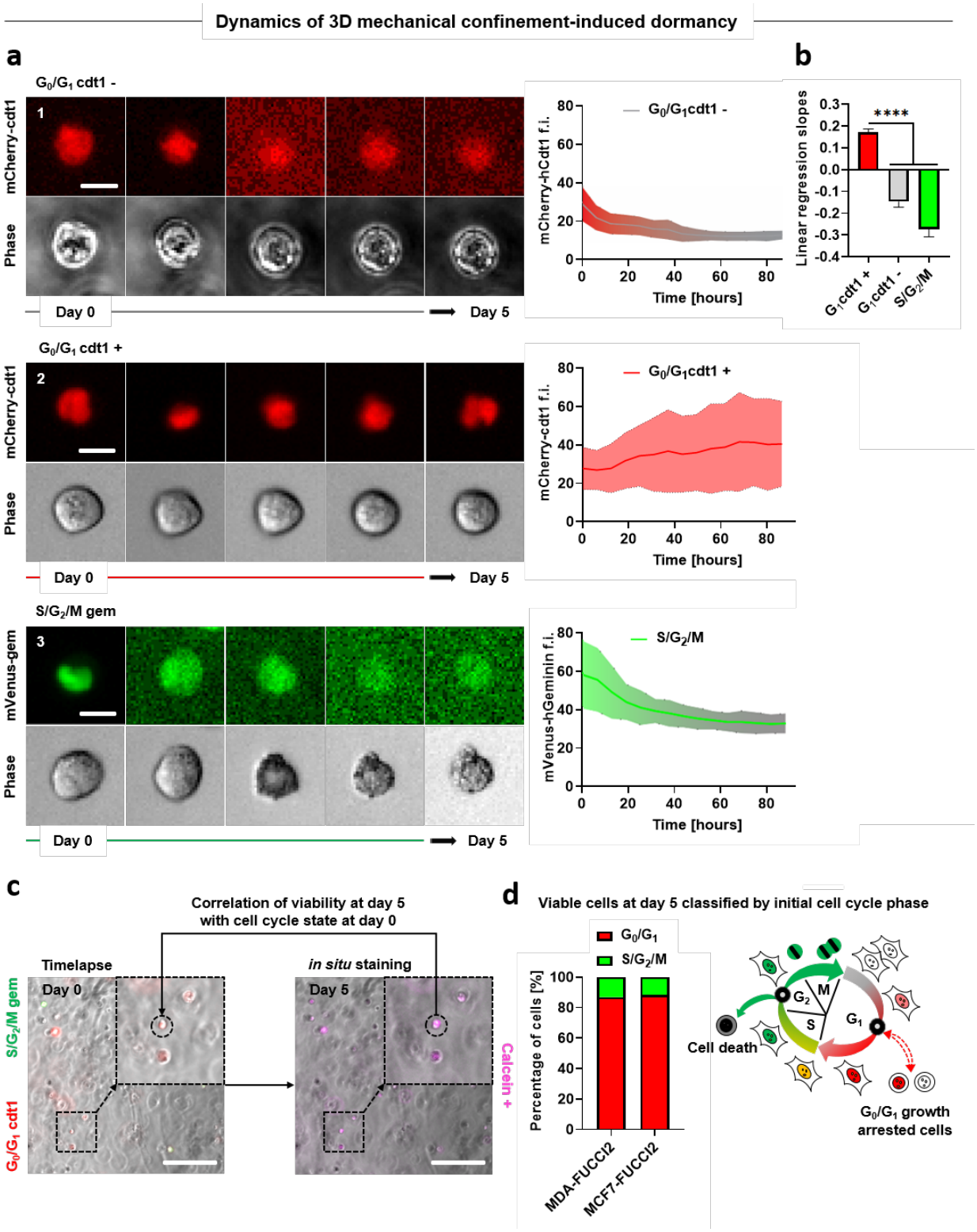

Fig. 2 Dynamics of cell cycle and viability correlation reveal that G_0/G_1 cells are substantially more resistant to 3D mechanical confinement than cells in the $S/G_2/M$ phase. a) Representative time lapse images of single MDA-FUCCI2 cells in 3D alginate stiff hydrogels with respective single cell longitudinal tracking of mCherry-hCdt1 and mVenus-hGeminin fluorescence intensity (f.i.). Center trace and shaded area indicate mean and standard deviation (n≥15 cells). Scale bar equals 10 µm. **b)** Comparison of linear

regression slopes from f.i. tracking graph. Kruskal–Wallis test with Dunn's correction ****$p<0.0001$. **c)** Experimental workflow for longitudinal correlation of FUCCI2 initial cell cycle state within 3D alginate stiff hydrogels and viability after 5 days of encapsulation. Cells were stained *in situ* for viability after 5 days time lapse and the selected cells (calcein+) were tracked back to their initial cell cycle state (time of encapsulation). Scale bar equals 200 µm. **d)** Percentage bar plots show fraction of viable cells with respect to their initial cell cycle state for MDA-FUCCI2 and MCF7-FUCCI2 cells ($n \geq 241$ cells pooled from 3 independent experiments). Diagram of cell cycle progression under 3D mechanical confinement, revealing growth arrest and higher resilience for cells in G_0/G_1 and death for cells in $S/G_2/M$. The cartoon was adapted from Sakaue-Sawano et al.[15], Copyright (2008), with permission from Elsevier.

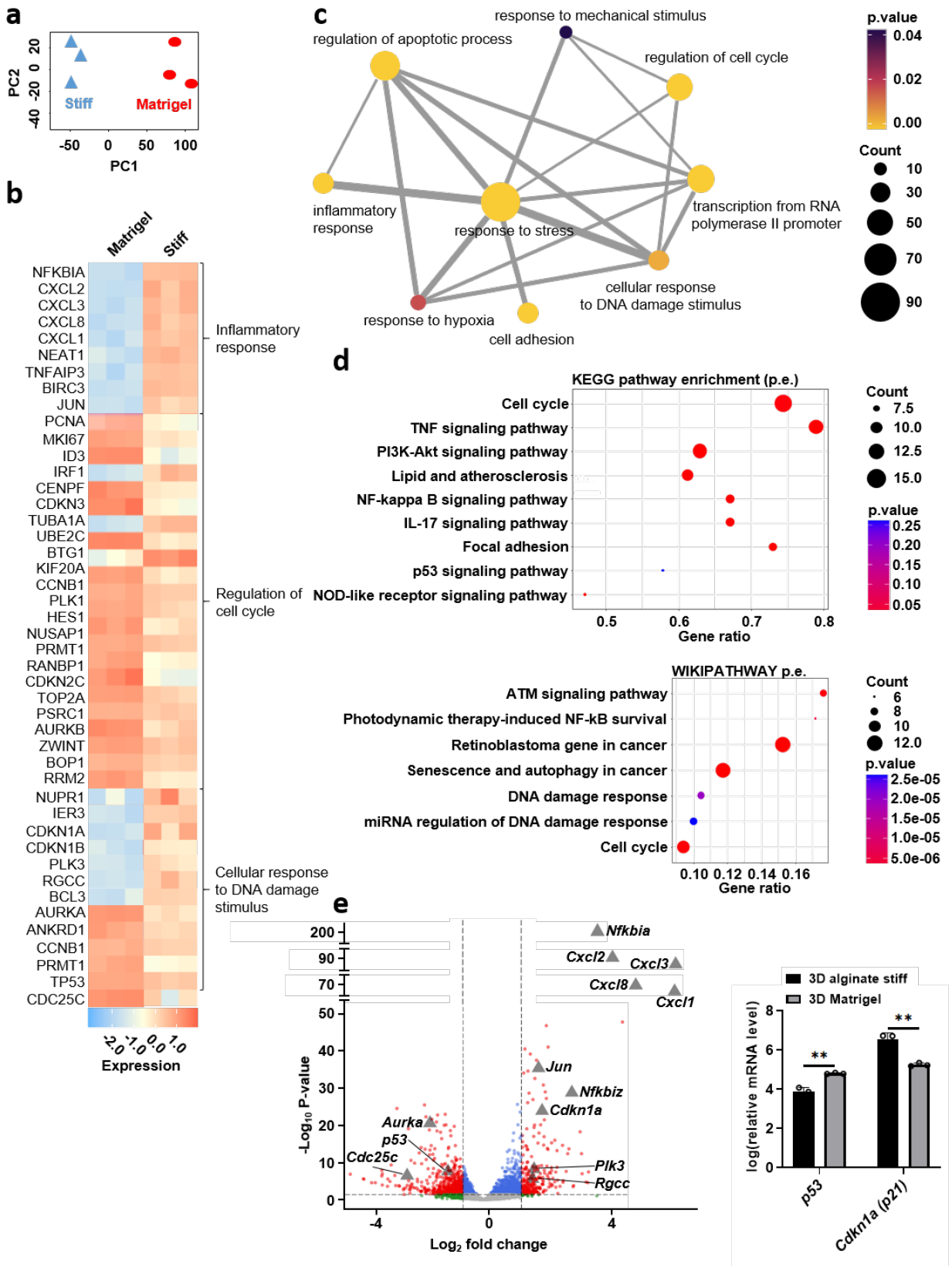

Fig. 3 Gene expression analysis of cells in 3D alginate stiff compared to 3D Matrigel. a) Principal-component analysis (PCA) based on all expressed genes between 3D alginate stiff and 3D Matrigel groups acquired from RNA sequencing (n=3 for each condition).

853 **b)** Heat map of selected differentially expressed genes involved in inflammatory response,
854 regulation of cell cycle and cellular response to DNA damage stimulus. **c)** Network map of
855 selected biological processes most enriched in 3D alginate compared to 3D Matrigel. Node
856 size, node color and edge width represent number of genes, *p*-value from enrichment
857 analysis and overlap of number of genes between two gene sets, respectively. **d)** Selected
858 top differentially regulated pathways from Gene-set-enrichment analysis (GSEA) on
859 differentially expressed genes between cells grown in 3D alginate stiff and 3D Matrigel
860 according to KEGG and WIKIPATHWAY databases. **e)** Volcano plot of differentially
861 expressed genes between 3D alginate stiff and 3D Matrigel. Grey triangles mark genes of
862 interest associated with inflammation and DNA-damage pathways (grey dots=not
863 significant, green dots= significant absolute log(base2) fold change of > 1, blue dots=
864 significant *p-value* of < 0.05, red=significant absolute log(base2) fold change of > 1 and *p-*
865 *value* <0.05 from a total of 9426 entries). Relative mRNA levels of p53 and cdkn1a (p21)
866 (n=3 for each condition). Student's *t*-test **p≤0.01. Error bars indicate mean and standard
867 deviation.

868

869

870

871

872

873

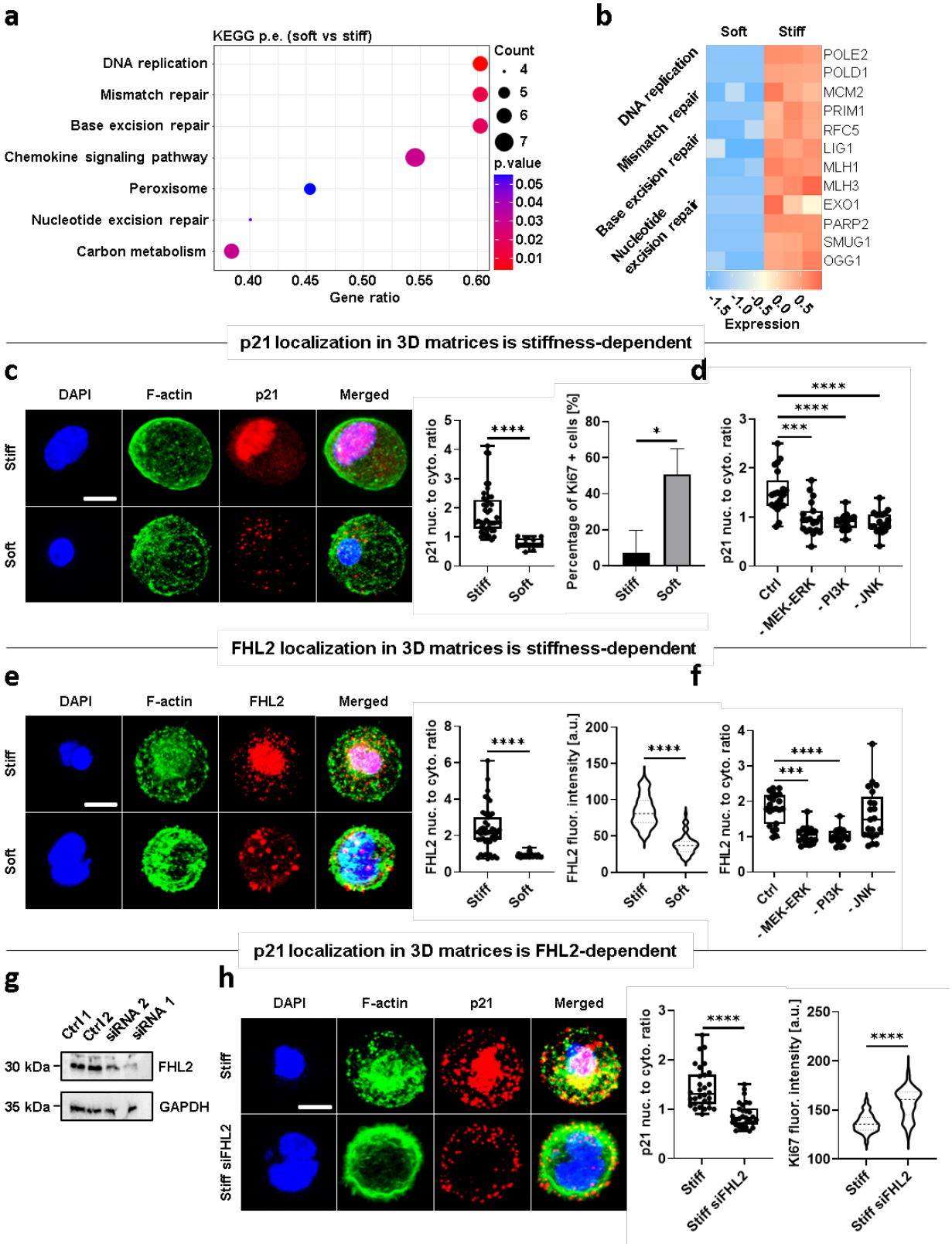

Fig. 4 p21 and FHL2 localization in 3D matrices is stiffness-dependent and FHL2 mediates p21 localization and Ki67 expression. a) Selected top differentially regulated pathways from GSEA based on differentially expressed genes between cells grown in soft vs. stiff alginate hydrogels. **b)** Heat map of differentially expressed genes (soft vs. stiff)

from DNA damage and repair pathways. **c)** Representative confocal images of p21 localization and quantification of its nuclear-to-cytoplasmic ratio (n=3 gels for 10 to 42 cells) for MDA231 cells within 3D stiff and soft alginate hydrogels after 7 days of encapsulation (blue=DAPI, green=F-Actin, red=p21). Scale bar equals 10 µm, Mann-Whitney *U*-test ****p<0.0001. Fraction of Ki67-positive cells (n=3 gels for 28 to 628 cells), student's *t*-test *p<0.05. **d)** Quantification of p21 localization in 3D alginate stiff hydrogels after 7 days in the presence or absence of indicated inhibitors (n≥19 cells). Student's *t*-test with respect to control group (3D alginate stiff) ***p<0.001 and ****p<0.0001. **e)** Representative confocal images of FHL2 localization and quantification of its nuclear-to-cytoplasmic ratio (n=3 gels for 36 to 46 cells) for MDA231 cells within 3D stiff and soft alginate hydrogels after 7 days of encapsulation (blue=DAPI, green=F-Actin, red=FHL2). Scale bar equals 10 µm, Mann-Whitney *U*-test ****p<0.0001. FHL2 fluorescence intensity (f.i.) per cell (n=3 gels for 59 to 151 cells) Mann-Whitney *U*-test ****p<0.0001. **f)** Quantification of FHL2 localization in 3D alginate stiff hydrogels after 7 days in the presence or absence of indicated inhibitors (n≥18 cells). Student's *t*-test with respect to control group (3D alginate stiff) ***p<0.001 and ****p<0.0001. **g)** Immunoblot showing FHL2 levels in MDA231 cells treated with two different anti-FHL2 siRNA oligos compared to untreated (control 1) or scramble (control 2) groups. GAPDH, glyceraldehyde-3-phosphate de-hydrogenase. **h)** Representative confocal images of p21 localization and quantification of its nuclear-to-cytoplasmic ratio (n=3 gels for 30 cells) for MDA231 normal and siRNA-FHL2 silenced cells within 3D stiff alginate hydrogels (blue=DAPI, green=F-Actin, red=p21). Scale bar equals 10 µm, Mann-Whitney *U*-test ****p<0.0001. Ki67 f.i. per cell (n= 74 to 260 cells), Mann-Whitney *U*-test ****p<0.0001. Datasets shown as box plots with median for 25th to 75th percentiles and whiskers for minimum and maximum. Violin plots show dashed lines for median and dotted lines for the two quartile lines. Error bars indicate mean and standard deviation.

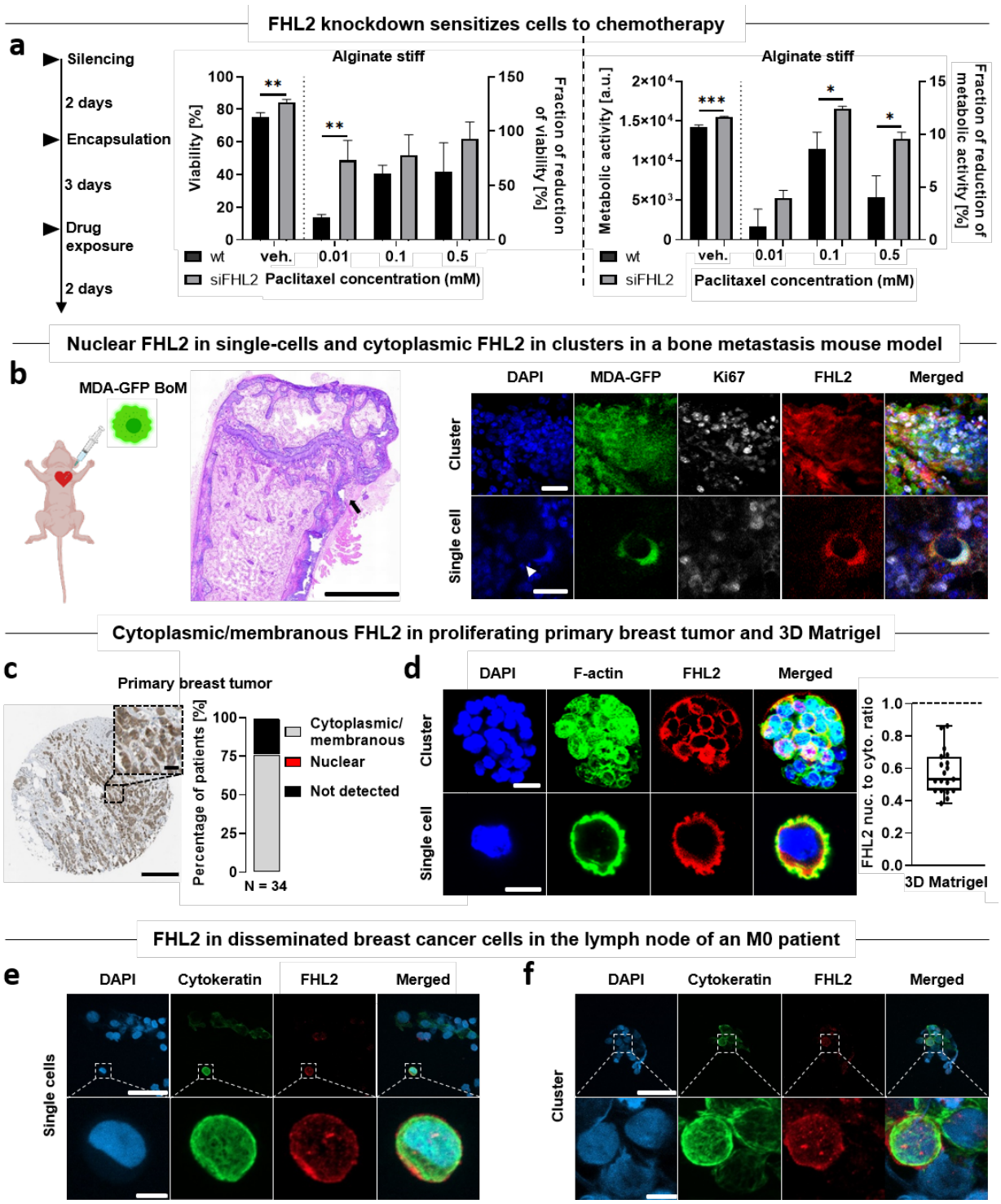

Fig. 5 FHL2 knockdown sensitizes cells to chemotherapy. FHL2 expression and localization in murine tissue of a breast cancer bone metastasis model, in human primary breast tumor and in early DCCs of an M0 patient. a) FHL2-silenced MDA231 cells were encapsulated for 3 days and exposed to Paclitaxel (0.01 to 0.5 mM) for 2 days, after which viability and metabolic activity (Presto Blue) measurements of normal and siRNA-FHL2 silenced cells within 3D alginate stiff were performed. Left y-axis corresponds to the overall viability and metabolic activity of vehicle (untreated groups). Right y-axis shows the fraction of reduction of viability and metabolic activity of drug treated groups with respect to the untreated group. Student's *t*-test (n=3 hydrogels) *p≤0.05,

919 **p≤0.01, ***p≤0.001, ****p≤0.0001. Error bars indicate mean and standard deviation.
920 **b)** Intracardiac injection of GFP-tagged MDA-MB-231-1883 BoM cells in mice with
921 representative Hematoxylin and Eosin (H&E) staining of the femur showing an osteolytic
922 lesion (arrowhead). Representative confocal images of Ki67 (proliferation) and FHL2
923 localization of GFP-tagged MDA-MB-231-1883 BoM cells as single cells and clusters.
924 Scale bars equal 1000 µm, 25 µm and 20 µm for H&E overview, cluster and single cell
925 images, respectively. **c)** Representative immunohistochemical image of FHL2 localization
926 in a female patient (50 years old) with breast ductal carcinoma. Fraction of FHL2
927 localization in 34 patients with primary breast ductal carcinoma. Data obtained from The
928 Human Protein Atlas[58]. Scale bar equals 20 µm. **d)** Representative confocal images of FHL2
929 localization in spheroids and single MDA231 cells within 3D Matrigel after 7 days of
930 encapsulation and quantification of its nuclear-to-cytoplasmic ratio (n=19 cells)
931 (blue=DAPI, green=F-Actin, red=FHL2). Scale bar equals 20 µm for spheroid image and
932 10 µm for single cell image. **e, f)** Confocal images of cytokeratin (epithelial marker) and
933 FHL2 (in single cells and within clusters) of human breast cancer cells disseminated in the
934 sentinel lymph node of an M0 patient. Scale bars equal 50 µm and 5 µm for the wide and
935 zoomed images, respectively.
936
937
938
939
940
941
942
943
944
945
946
947
948
949
950
951

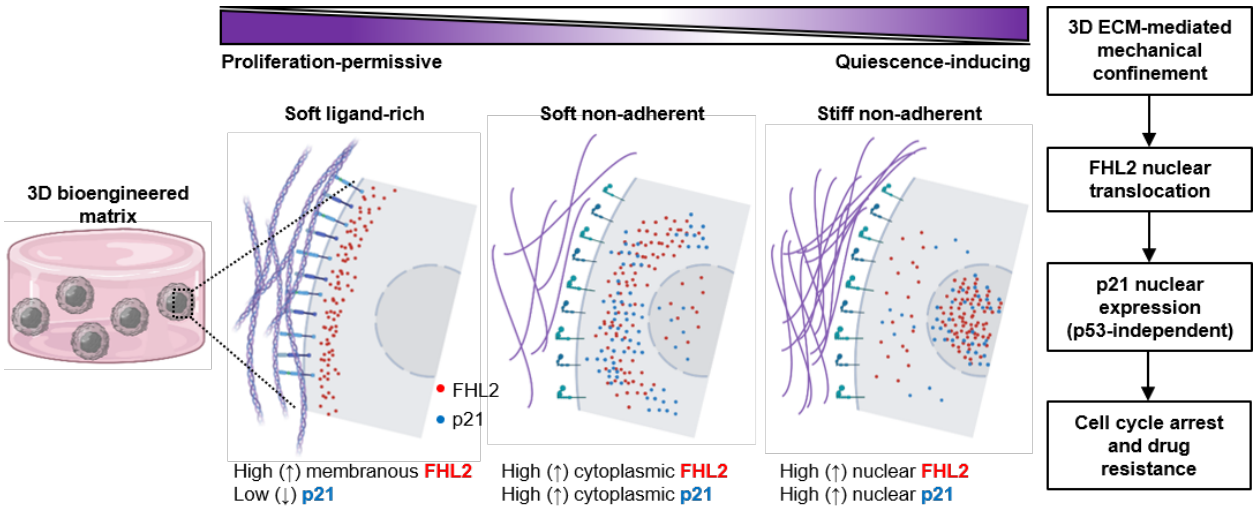

Fig. 6 Proposed stiffness-mediated FHL2 signaling mechanism in 3D bioengineered matrices inducing cancer cell quiescence and drug resistance. In proliferation-permissive, ligand-rich microenvironments such as basement membranes, stronger adhesion sites maintain FHL2 in the membranous regions. In low or non-adherent microenvironments, the increase in mechanical confinement (stiffness) results in FHL2 translocation to the nucleus, leading to high p21 nuclear expression and cell cycle arrest (graphical illustration created with BioRender.com).